Blast-wave-Tsallis-power model for p_T spectra and elliptic flow v_2 of hadrons in collisions of identical nuclei at energies available at the CERN Large Hadron Collider

Smbat Grigoryan *
Joint Institute for Nuclear Research, 141980 Dubna, Russia
and A.I.Alikhanyan National Science Laboratory (YerPhI) Foundation, 0036 Yerevan, Armenia

(Received 3 September 2025; revised 28 October 2025; accepted 20 November 2025; published 8 January 2026)

A generalization of the phenomenological blast-wave-Tsallis-power model, recently proposed by the author for the hadrons' transverse momentum (p_T) spectra measured at the CERN Large Hadron Collider (LHC), is developed to also describe the hadrons' p_T-differential elliptic flow coefficients v_2 in identical nuclei collisions of different centralities. The model describes well the available data on p_T spectra and v_2 for any p_T of various particles, from pions to charmonia, in Pb-Pb collisions at $\sqrt{s_{NN}} = 2.76$ and 5.02 TeV and in Xe-Xe collisions at $\sqrt{s_{NN}} = 5.44$ TeV. Also, predictions for OO collisions at $\sqrt{s_{NN}} = 5.36$ TeV are given. While the model is mainly targeting the energies available at the LHC, it also works at much lower energies available at the BNL Relativistic Heavy Ion Collider.

DOI: 10.1103/yb33-p593

I. INTRODUCTION

Recently, the phenomenological blast-wave-Tsallis-power model (BWTPM) was proposed, which describes quite accurately the midrapidity p_T spectra of various hadrons in the whole p_T range measured in pp and Pb-Pb collisions at the CERN Large Hadron Collider (LHC) [1]. These p_T spectra are integrated over the hadron azimuthal angle φ. They depend strongly on the collision centrality and center-of-mass energy per nucleon-nucleon pair, $\sqrt{s_{NN}}$. BWTPM has three terms including a standard blast-wave model (BWM) term [2] to account for the hydrodynamic radial flow and kinetic freeze-out effects, a term in the Tsallis (Ts) distribution form [3,4], responsible for the contribution from the resonance decays, and a power-law (Po) term describing the QCD hard processes. As shown in Ref. [1], the model parameters depend generally on the collision system (pp or Pb-Pb), but some of them are independent of the $\sqrt{s_{NN}}$ or the particle type or the collision centrality.

In the present paper, a generalization of the BWTPM is developed to describe, in addition to the p_T spectra, also the midrapidity elliptic flow coefficients v_2 in identical nuclei (AA) collisions. The v_2 coefficients characterize the azimuthal asymmetry of hadron momentum distribution and depend on hadron type, p_T, collision system, and centrality. The asymmetry is driven mainly by an almond shape (in the plane transverse to the collision axis) of the hadronic medium (quark-gluon plasma) created in noncentral collisions. Due to this shape, the in-medium pressure gradient and radial flow velocity become anisotropic resulting in the anisotropy of the hadron momentum spectra [5]. Following Ref. [6], I use the generalized BWM with a transversally anisotropic freeze-out hypersurface of elliptical shape, instead of the isotropic circular one considered in Refs. [1,2]. For the hadronic medium radial flow velocity I assume similar azimuthal dependence as in Refs. [6,7]. Also, the other two therms of BWTPM are modified by including a simple dependence on φ. Having redefined so the model, the hadron v_2 can be determined as the second coefficient in the Fourier series of its invariant yield $\mathrm{d}^3N/(p_T\mathrm{d}p_T\mathrm{d}y\,\mathrm{d}\varphi)$ [6–10]:

$$v_2 = \int_0^{2\pi} d\varphi \cos(2\varphi) \frac{\mathrm{d}^3N}{\mathrm{d}p_T\mathrm{d}y\,\mathrm{d}\varphi} \Big/ \int_0^{2\pi} d\varphi \frac{\mathrm{d}^3N}{\mathrm{d}p_T\mathrm{d}y\,\mathrm{d}\varphi}, \qquad (1)$$

where y is the hadron rapidity. The v_2 contribution dominates in this series for noncentral collisions.

The next objective of the present paper is to reduce strongly the number of the BWTPM parameters by parametrizing their dependence on the collision system, centrality, energy, and on the particle type and p_T using simple formulas. As a measure of collision centrality, the corresponding charged-particle multiplicity density at midrapidity (η is pseudorapidity),

$$M_{\mathrm{ch}} \equiv \langle \mathrm{d}N_{\mathrm{ch}}/\mathrm{d}\eta \rangle_{\eta=0} \qquad (2)$$

is used; it serves as a good scaling variable for the comparison of hadron production mechanisms in different collision systems (see, e.g., the ALICE review paper [11]). These parametrizations increase significantly the predictive power of the model. Furthermore, I propose another simplification of the BWTPM. While in Ref. [1] it had two different functional

*Contact author: Smbat.Grigoryan@cern.ch

Published by the American Physical Society under the terms of the Creative Commons Attribution 4.0 International license. Further distribution of this work must maintain attribution to the author(s) and the published article's title, journal citation, and DOI. Funded by SCOAP³.

forms for $p_{\rm T} \leqslant 40$ GeV and $p_{\rm T} > 40$ GeV, it now has the same form for any $p_{\rm T}$.

The values of the BWTPM parameters are obtained then from a simultaneous fit of the combined data on different hadron $p_{\rm T}$ spectra and v_2 measured mostly by the ALICE experiment in Pb-Pb and Xe-Xe collisions at the LHC. In addition to the hadrons considered in Ref. [1] ($\pi^{\pm}$, π^0, $K^{\pm}$, $K^0_{\rm S}$, p, $\overline{p}$, K^{*0}, $\overline{K}^{*0}$, ϕ, Λ, $\overline{\Lambda}$, Ξ^-, $\overline{\Xi}^+$, Ω^-, $\overline{\Omega}^+$, D^0, $D^{\pm}$, J/ψ, and unidentified charged particles), the η, ρ^0 mesons and Λ_c^+, $\overline{\Lambda}_c^-$baryons are included too. It is assumed that a particle and its antiparticle have the same $p_{\rm T}$ spectrum and v_2. While in the LHC energy domain, which is the main target of present study, this assumption is perfectly valid, it could be violated at much lower energies. To test the model at such energies, I included in the simultaneous fit also some limited data on $p_{\rm T}$ spectra and v_2 measured at the BNL Relativistic Heavy Ion Collder (RHIC).

Note that the previous similar simultaneous fits of the LHC data on hadrons' $p_{\rm T}$ spectra and v_2 were done mainly at low $p_{\rm T}$ ($p_{\rm T} \lesssim 3\,{\rm GeV}/c$) [7,11,12] using various generalizations of the BWM. The present model, due to its additional power-law terms, is able to describe much larger data sets in the whole available $p_{\rm T}$ region.

The paper is organized as follows. Section II gives details of the generalized BWTPM. Section III presents a parametrization for the $M_{\rm ch}$ data measured in various AA collisions. Section IV describes parametrizations for the model parameters dependence on the AA collision characteristics and the particle type and $p_{\rm T}$. In Sec. V the model free parameters are determined from the simultaneous fit of all the used data. In Sec. VI the results and predictions are discussed. Conclusions are given in the last section.

II. DESCRIPTION OF BWTPM

The present model consists of three terms that generalize the similar terms of Ref. [1]. The first (BW) term corresponds to the generalized BWM [6] and two others (named Ts and Po as in Ref. [1]) include additionally the second Fourier coefficients $v_{2t}(p_{\rm T})$ and $v_{2p}(p_{\rm T})$, respectively, to account for the elliptic flow. Thus, for a particle's φ-dependent $p_{\rm T}$ spectrum in AA collisions at midrapidity, where it can be considered independent of the rapidity y, I propose the following model:

$$\frac{{\rm d}^3N}{{\rm d}p_{\rm T}{\rm d}y\,{\rm d}\varphi} \equiv F_\varphi, \tag{3}$$

$$\begin{aligned} F_\varphi(p_{\rm T}) = \frac{g}{2\pi^3}\frac{f_N}{f_S}p_{\rm T}m_{\rm T}\Bigg[& f_{\rm BW}V\int_0^1 \hat{r}\,d\hat{r}\int_0^{2\pi}\frac{d\phi}{2\pi} \\ & \times K_1\left(\gamma_{\rm T}\frac{m_{\rm T}}{T}\right)\exp\left(\gamma_{\rm T}\beta_{\rm T}\frac{p_{\rm T}}{T}\cos(\varphi-\phi_b)\right) \\ & + f_1V_1[1+2v_{2t}(p_{\rm T})\cos(2\varphi)]\left(1+\frac{m_{\rm T}}{c_1e_1n}\right)^{-c_1n} \\ & + f_2V_2[1+2v_{2p}(p_{\rm T})\cos(2\varphi)]\left(c_2^2+\frac{p_{\rm T}^2}{e_2^2}\right)^{-\frac{n}{2}}\Bigg], \end{aligned} \tag{4}$$

where N is the particle yield per collision event, $g = 2J+1$ is its spin degeneracy factor, $m_{\rm T} = \sqrt{m^2+p_{\rm T}^2}$ is its transverse mass, $\gamma_{\rm T} = 1/\sqrt{1-\beta_{\rm T}^2}$, $\beta_{\rm T}$ is the hadronic medium radial (transverse) flow velocity at the kinetic freeze-out,

$$\beta_{\rm T} = \tanh\rho, \quad \rho = [\rho_0 + \rho_2\cos(2\phi_b)]\hat{r}^k, \tag{5}$$

ρ is the flow rapidity with the second order anisotropy ρ_2 and profile exponent k, $V = \pi R_xR_y\tau_f$ is the volume of this medium with transverse sizes R_x and R_y, τ_f and T are its proper lifetime and temperature, and K_1 is a modified Bessel function of the second kind. Note that $\tanh\rho_0$ is equal to $\beta_{\rm s}$ used in Ref. [1]. The global normalization parameter f_N is close to unity at LHC energies but could depend on the normalization conditions of the used data obtained in different experiments. Its energy dependence is significant at lower RHIC energies and will be specified in Sec. IV. Parameter f_S is equal to unity (as in Ref. [1]) for ordinary hadrons consisting of up and down quarks only. But for hadrons containing strange or heavier quarks it is greater than unity and quantifies the suppression of their yields depending on the hadron type, $p_{\rm T}$, and collision centrality. It describes the observed enhancement of the relative yields of such hadrons with respect to ordinary ones when going from peripheral to central collisions (i.e., from small to large $M_{\rm ch}$) [11]. The explicit form of f_S is specified in Sec. IV.

The azimuthal dependence of $\beta_{\rm T}$ in Eq. (5) is similar to the one in Refs. [6,7], while its dependence on radial variable $\hat{r}$ is defined for arbitrary k [1,2] and varies strongly with the collision centrality ($k = 1$ in Refs. [6,7]). The meaning of azimuthal angles ϕ_b and ϕ and their interrelation

$$\tan\phi_b = \sqrt{r_{xy}}\tan\phi, \quad r_{xy} \equiv R_x^2/R_y^2 \tag{6}$$

are explained in Refs. [6,7]. In the present model, three parameters R_x, R_y, and τ_f enter into two independent combinations via parameters V and $r_{xy} \leqslant 1$.

The important quantities for the elliptic flow v_2 are ρ_2, r_{xy} [6,7], k, and functions $v_{2t}(p_{\rm T})$ and $v_{2p}(p_{\rm T})$ in Eq. (4), though T and ρ_0 also influence the $p_{\rm T}$ dependence of v_2 [6]. From hydrodynamic models and experimental data it follows that there is an approximately linear relation between v_2 and the eccentricity ε_2 of the collision geometry [13–16], which can be defined in the present model as

$$\varepsilon_2 = (1-r_{xy})/(1+r_{xy}). \tag{7}$$

Moreover, in the generalized BWM [6] with $\rho_2 = 0$ one gets $v_2 = \varepsilon_2/2$. I have checked by fitting the v_2 data that parameter ρ_2 as well as the functions $v_{2t}(p_{\rm T})$ and $v_{2p}(p_{\rm T})$ have centrality dependence similar to ε_2. For the model's simplicity, I assume that they are proportional to ε_2. Their explicit forms will be specified in Sec. IV. All other parameters in Eq. (4) have the same meaning as in Ref. [1]. Note that parameters $f_{\rm BW}$, f_1, f_2, c_1, and c_2 are the same for any AA collision system and depend only on the particle type.

Now, integration of Eq. (3) by φ gives

$$\frac{\mathrm{d}^2N}{\mathrm{d}p_\mathrm{T}\mathrm{d}y} \equiv F, \tag{8}$$

$$F(p_\mathrm{T}) = \frac{g}{\pi^2}\frac{f_N}{f_S}p_\mathrm{T}m_\mathrm{T}\Bigg[f_\mathrm{BW}V\int_0^1 \hat{r}\,d\hat{r}\int_0^{2\pi}\frac{d\phi}{2\pi} \times K_1\left(\gamma_\mathrm{T}\frac{m_\mathrm{T}}{T}\right)I_0\left(\gamma_\mathrm{T}\beta_\mathrm{T}\frac{p_\mathrm{T}}{T}\right) + f_1V_1\left(1+\frac{m_\mathrm{T}}{c_1e_1n}\right)^{-c_1n} + f_2V_2\left(c_2^2+\frac{p_\mathrm{T}^2}{e_2^2}\right)^{-\frac{n}{2}}\Bigg]. \tag{9}$$

Performing a similar integration in Eq. (1), one finds (see also Ref. [7])

$$v_2(p_\mathrm{T}) = \frac{g}{\pi^2}\frac{f_Np_\mathrm{T}m_\mathrm{T}}{f_SF(p_\mathrm{T})}\Bigg[f_\mathrm{BW}V\int_0^1 \hat{r}\,d\hat{r}\int_0^{2\pi}\frac{d\phi}{2\pi}\cos(2\phi_b) \times K_1\left(\gamma_\mathrm{T}\frac{m_\mathrm{T}}{T}\right)I_2\left(\gamma_\mathrm{T}\beta_\mathrm{T}\frac{p_\mathrm{T}}{T}\right) + f_1V_1v_{2t}(p_\mathrm{T})\left(1+\frac{m_\mathrm{T}}{c_1e_1n}\right)^{-c_1n} + f_2V_2v_{2p}(p_\mathrm{T})\left(c_2^2+\frac{p_\mathrm{T}^2}{e_2^2}\right)^{-\frac{n}{2}}\Bigg]. \tag{10}$$

I_0 and I_2 in Eqs. (9) and (10) are modified Bessel functions of the first kind. So, one finds Eqs. (8)–(10) for hadrons' p_T spectrum and elliptic flow, respectively. They can be used to describe the corresponding data for different identified particles. There are also similar data sets for the unidentified charged particles, which are a mixture of the $\pi^\pm$, $K^\pm$, p, $\overline{p}$, and charged hyperons. These data have usually much larger p_T range than the ones for the identified particles. Charged-particle p_T spectra can be defined, assuming the same spectrum for a particle and its antiparticle, by the equations [1]

$$\frac{\mathrm{d}^3N_\mathrm{ch}}{\mathrm{d}p_\mathrm{T}\mathrm{d}\eta\,\mathrm{d}\varphi} = 2\left(\sum_{i=\pi,K,p}\frac{p_\mathrm{T}}{m_{\mathrm{T},i}}F_{\varphi,i} + f_\mathrm{hyp}\frac{p_\mathrm{T}}{m_{\mathrm{T},p}}F_{\varphi,p}\right), \tag{11}$$

$$\frac{\mathrm{d}^2N_\mathrm{ch}}{\mathrm{d}p_\mathrm{T}\mathrm{d}\eta} = 2\left(\sum_{i=\pi,K,p}\frac{p_\mathrm{T}}{m_{\mathrm{T},i}}F_i + f_\mathrm{hyp}\frac{p_\mathrm{T}}{m_{\mathrm{T},p}}F_p\right). \tag{12}$$

Here, the functions $F_{\varphi,i}$ and F_i are defined by Eqs. (4) and (9), respectively. The factors 2 account for the positive and negative particles and factors $p_\mathrm{T}/m_\mathrm{T}$ account for the change from rapidity to pseudorapidity at midrapidity ($d\eta/dy \approx p_\mathrm{T}/m_\mathrm{T}$). The last terms in Eqs. (11) and (12) describe approximately the small contribution of hyperons via the proton contribution, scaled by parameter f_hyp. Using Eqs. (11) and (1) and performing integration by φ one can find easily the analog of Eq. (10) for the unidentified charged particles. Note that Eqs. (8), (9), and (12) for the p_T spectra are similar to the corresponding ones in Ref. [1] if $f_N = f_S = 1$ and $\rho_2 = 0$.

It was checked that the presented generalized BWTPM is able to fit the LHC data on midrapidity hadron p_T spectra and v_2 in Pb-Pb and Xe-Xe collisions with a good accuracy, similar to that achieved in Ref. [1]. However, as in Ref. [1], the number of the model free parameters is too big, which reduces the model's predictive power. It is mostly due to the ten centrality-dependent parameters $V, V_1, V_2, T, k, e_2, n, f_S, r_{xy}$, and ρ_0, which generally can depend also on p_T, the collision system, and $\sqrt{s_{NN}}$ (f_S depends on particle species too). A typical number of ALICE centrality classes for Pb-Pb data at $\sqrt{s_{NN}} = 2.76$ TeV [17] and 5.02 TeV [18] as well as for Xe-Xe data at $\sqrt{s_{NN}} = 5.44$ TeV [19] is about 10 in each case. So, to describe these combined data, one needs to fit $10(10 + 10 + 10) = 300$ independent values for the mentioned ten parameters. Taking into account also the RHIC data included in the present study, this number of independent values becomes more than 600. To reduce the number of free parameters strongly, these ten (and other) parameters are parametrized using the charged-particle multiplicities M_ch, which depend on the collision system, centrality, and $\sqrt{s_{NN}}$, and are well known experimentally for various AA collisions [17–22]. The key assumption of the present paper is that all the centrality dependence in BWTPM can be expressed via M_ch only. It is motivated by the experimental observation that any hadron species has similar p_T spectra in different AA collisions with the same M_ch and $\sqrt{s_{NN}}$ (see an example of such a similarity for K^{*0} meson p_T spectra in Ref. [23]). To have a more general and predictive approach, I will use not the experimental values of M_ch (which can be missing for some centralities) but their accurate parametrization, valid for any AA collision centrality and energy. This parametrization is presented in the next section.

III. PARAMETRIZATION OF M_ch

The mean value of charged-particle multiplicity density at midrapidity M_ch [defined in Eq. (2)] is one of the main characteristics of nucleus-nucleus collisions. Its dependence on the collision system, centrality, and $\sqrt{s_{NN}}$ was measured for different AA collisions at LHC [17–20] and RHIC [21,22] energies. Centrality is commonly expressed in percentiles or fractions x_c of the total nucleus-nucleus cross section [11] (centrality in % is equal to $100x_c$). Here I propose a simple parametrization for the M_ch data [17–22] versus atomic mass number A, collision centrality fraction x_c, and energy $\sqrt{s_{NN}}$. It relates M_ch with the similar quantity $M_\mathrm{ch}^{pp} \equiv \langle \mathrm{d}N_\mathrm{ch}^{pp}/\mathrm{d}\eta\rangle_{\eta=0}$ of the inelastic pp collisions at energy $\sqrt{s} = \sqrt{s_{NN}}$. For M_ch^{pp} I used the data measured at the LHC [24–26] as well as at lower energies [21,27] and parametrized their energy dependence. The M_ch and M_ch^{pp} data were obtained by averaging the respective multiplicity distribution on pseudorapidity in the range $|\eta| < 0.5$ [17–20,22,24–26] or $|\eta| < 1$ [21,27]. Within the data uncertainties both ranges give similar results [26]. Parameters of the parametrization are obtained via a simultaneous fit of the M_ch and M_ch^{pp} data using the combined fit technique of the root framework [28], which gives $\chi^2/\mathrm{NDF} = 54.1/155$. The fit results are shown in Figs. 1 and 2, and the parametrization has

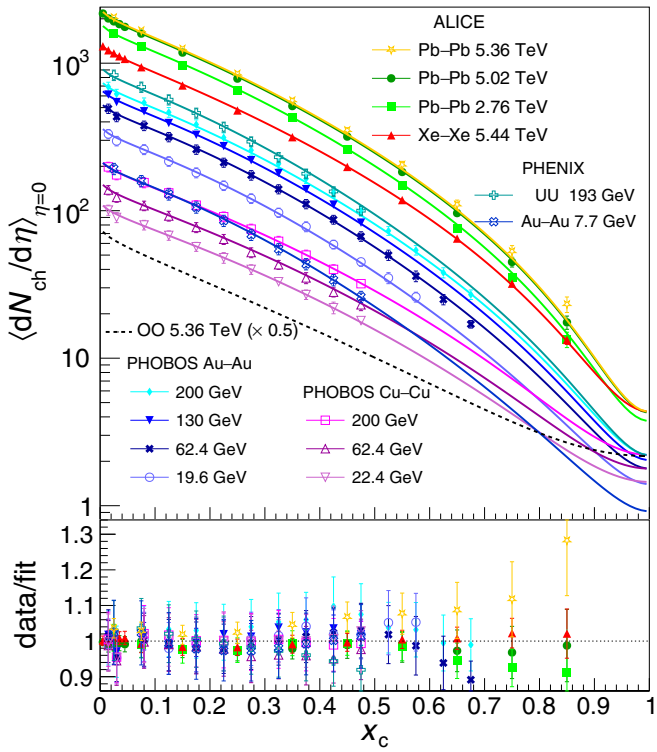


FIG. 1. Fit of the midrapidity charged-particle multiplicity density data measured for various AA collisions at different centralities x_c and energies $\sqrt{s_{NN}}$ by the ALICE [17–20], PHOBOS [21], and PHENIX [22] experiments. The dashed line shows the prediction (multiplied by 0.5 for better visibility) for the OO collisions at $\sqrt{s_{NN}} = 5.36$ TeV. The data/fit ratio demonstrates the quality of the fits.

the form

$$\frac{M_{\rm ch}}{M_{\rm ch}^{pp}} = 1 + (A-1)^{1+0.00013y} \frac{\left(1-x_c^2\right)^{2+0.0018y\alpha}}{\left(x_c^{\delta}+\beta\right)^{2.1}\gamma}, \quad (13)$$

$$M_{\rm ch}^{pp} = 0.615 \frac{1+(\sqrt{s_{NN}}/e_0)^{0.258}}{1+(e_0/\sqrt{s_{NN}})^2}, \quad (14)$$

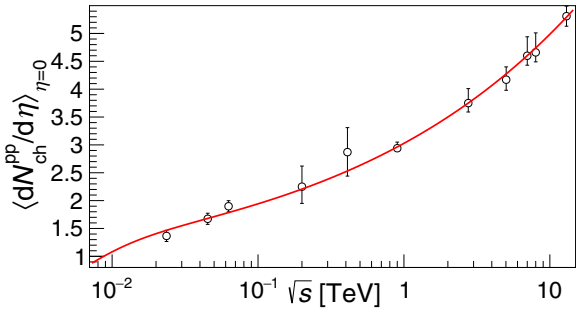


FIG. 2. Fit of the midrapidity charged-particle multiplicity density in inelastic pp collisions by Eq. (14) as a function of $\sqrt{s}$. Six higher energy data points are from Refs. [24–26] and the remaining data points are from Refs. [21,27].

where $\alpha = \ln\left(\frac{17.4}{\sqrt{s_{NN}}}\right)$, $\beta = \left(\frac{0.0027}{\sqrt{s_{NN}}}\right)^{0.054}$, $\delta = A^{0.063}$, $\gamma = 1 + 1.22x_c^{0.47}$, $y = A(1-x_c)$, and $e_0 = 0.005$ TeV (everywhere in the present paper, if it is not specified otherwise, $\sqrt{s_{NN}}$ is defined in units of TeV). The bottom panel of Fig. 1 demonstrates that Eq. (13) describes most of the data points with better than 10% accuracy. However, it underestimates the ALICE recent data for the most peripheral Pb-Pb collisions at 5.36 TeV [20]. This could be due to the new centrality calibration [20], since all other ALICE data are described well. One can expect that Eq. (13) would give accurate values of $M_{\rm ch}$ also for new AA collisions. The result for oxygen-oxygen (OO) collisions, carried out at the LHC in July 2025, is also shown in Fig. 1. Note that for $A = 1$ or for the most peripheral collisions, when $x_c \to 1$, the right-hand side of Eq. (13) equals unity. For the most central collisions, when $x_c \to 0$, one obtains a very simple formula for the maximal values of $M_{\rm ch}$ versus A and $\sqrt{s_{NN}}$:

$$\frac{M_{\rm ch}^{\rm max}}{M_{\rm ch}^{pp}} = 1 + (A-1)^{1+0.00013A}\left(\frac{\sqrt{s_{NN}}}{0.0027}\right)^{0.1134}. \quad (15)$$

For example, $M_{\rm ch}^{\rm max} = 2404$ (2457) for Pb-Pb collisions at $\sqrt{s_{NN}} = 5.02$ (5.36) TeV. It is worth noting that Eq. (13) should be used with caution since it gives the same $M_{\rm ch}$ for collisions of isobars of the same A [29].

To my knowledge, there is no generic parametrization in the literature similar to Eq. (13). The existing parametrizations of $M_{\rm ch}$ versus x_c (or versus the number of participant nucleons $N_{\rm part}$) are valid only for a particular AA collision system [21,30]. Of course, there are many sophisticated models describing the $M_{\rm ch}$ data, most of which use the hydrodynamical approach for particle production in AA collisions (see, e.g., Ref. [31]). However, such models are much more complex with respect to the simple parametrization of Eq. (13) and their accuracy is worse.

IV. PARAMETRIZATION OF BWTPM

Here I present parametrizations for the model parameters versus $M_{\rm ch}$ [given by Eq. (13)], A, $\sqrt{s_{NN}}$, and the particle mass and $p_{\rm T}$. The parametrizations were chosen to be as simple as possible by examining the behavior of the model parameters versus the collision system, centrality, and energy, and using the results of Ref. [1] and other studies. For normalization parameters V, V_1, and V_2, to describe their strong increase with centrality [1] and taking into account the experimental fact that the hadron $p_{\rm T}$-integrated yields increase linearly with $M_{\rm ch}$ at $M_{\rm ch} > 100$ [32], the following parametrizations are assumed:

$$V = a_1 M_{\rm ch} \Big/ \left(1 + f_r M_{\rm ch}^{1/3}\frac{m}{m_{\rm T}}\right)^{a_4}, \quad V_1 = a_2 M_{\rm ch},$$
$$V_2 = a_3 M_{\rm ch}. \quad (16)$$

Here and throughout the present paper the parameters a_i, $i = 1, 2, 3, \ldots$ are fitting constants. Parameter f_r is nonzero for K^{*0} and ρ^0 only, and accounts for the suppression of the yields of these short-lived resonances at low $p_{\rm T}$ due to the rescatterings of their decay products in the hadronic medium.

The suppression is stronger for more central collisions, and scales with $M_{\rm ch}^{1/3}$ [11].

The decrease of parameters T and k with increase of centrality and of parameters e_2 and n with increase of centrality and $\sqrt{s_{NN}}$ [1] can be parametrized as follows:

$$T = a_5/(1 + a_6 \ln M_{\rm ch}), \quad k = a_7/(1 + a_8 M_{\rm ch}), \tag{17}$$

$$e_2 = a_9/(1 + a_{10} \ln \sqrt{s_{NN}}) - a_{11} \ln M_{\rm ch}, \tag{18}$$

$$n = h_n \left[\frac{a_{12}}{1 + a_{13} y \ln \sqrt{s_{NN}}} + \frac{1 + (a_{14}/\sqrt{s_{NN}})^{2y}}{(M_{\rm ch}/a_{15})^{a_{16}/(1+x^2)}} \right], \tag{19}$$

where $x = p_{\rm T}/[a_{17} \ln(10^3 \sqrt{s_{NN}})]$, $y = (p_{\rm T}/m_{\rm T})^{a_{18}(c_2-1)}$, and$h_n$ differs from unity only for the strange and charmed baryons and J/ψ ($\sqrt{s_{NN}}$ is in units of TeV). Parameter c_2 is given below in Eq. (27). The term with parameter a_{14} is introduced to describe the RHIC data. It is significant at LHC energies for $p_{\rm T} \ll m$ only. Note that n becomes independent of $M_{\rm ch}$ at high $p_{\rm T}$ where $x > 1$.

The factor f_S is equal unity for ordinary hadrons and increases with decreasing centrality (or $M_{\rm ch}$) for other hadrons. It is greater for hadrons containing larger numbers of strange and charm (anti)quarks, which are denoted by n_s and n_c, respectively. For example, $n_s = 1$ for K and η mesons, and $n_s = 2$ for the ϕ meson. A simple parametrization for f_S in AA collisions is found,

$$f_S = 1 + \frac{[a_{19} n_s + a_{20} n_c + a_{21}|B|(n_s + n_c)]^2}{\left(1 + p_{\rm T}^2/a_{22}^2\right)\sqrt{M_{\rm ch} + a_{23}}}, \tag{20}$$

which describes well the enhancement features of all considered hadrons containing at least one strange or charm (anti)quark ($n_s = n_c = 0$ for ordinary hadrons). The term proportional to the hadron baryon number B is introduced to better describe the production of hyperons. The same parameter a_{21} for strange and charmed baryons is assumed since the data used for the latter case are very limited. For the hadrons containing bottom quarks, not considered in the present study, Eq. (20) can be modified accordingly. Note that f_S tends to unity at $p_{\rm T} > a_{22}$. Hence, the ratios of different particle yields in the present model are independent of centrality at high $p_{\rm T}$, as in the data [11].

It is known that the $p_{\rm T}$ averaged v_2 increases when going from central to peripheral collisions, and then decreases for very peripheral collisions [11,16]. Also, the eccentricity ε_2 of the transverse geometry of the hadronic medium behaves similarly versus collision centrality. When going from central to peripheral collisions, this geometry goes from circular to elliptical and ε_2 increases. But the geometry goes again to circular and ε_2 decreases at very peripheral collisions, where on average only one nucleon-nucleon collision accurs [10,15]. So one can assume $v_2 \sim \varepsilon_2$. This parametrization of r_{xy} ensures such a centrality dependence for ε_2 [given by Eq. (7)]

$$r_{xy} = 1 - \frac{a_{24} A^{a_{25}}}{1 + a_{26}/x + a_{27} x^{a_{29}} + a_{28}[(1 - f_d)x]^{a_{30}}}, \tag{21}$$

where $x = A^{a_{25}}(z_c + y)/(1 + y)$, A is the atomic mass number, $z_c = M_{\rm ch}/M_{\rm ch}^{0\text{–}5\%}$ is the normalized multiplicity over the multiplicity of the 0–5% most central collisions $M_{\rm ch}^{0\text{–}5\%}$ [determined by Eq. (13) at $x_c = 0.025$], and its correction $y = (a_{31}/\sqrt{s_{NN}})^{a_{32}} z_c$ is needed mainly for the fit of v_2 data at RHIC energies. Parameter f_d is introduced to describe a slightly different centrality dependence of v_2 data in Xe-Xe collisions compared to all other collision systems considered in present study, for which $f_d = 0$ is used. The difference is related to the nonspherical (deformed) shape of the ^{129}Xe nucleus [33].

To describe the centrality and energy dependence of the hadrons' $p_{\rm T}$ spectra and also of the charged-particle average transverse momentum $\langle p_{\rm T} \rangle$ [34,35], particularly its local minimum at $z_c \approx 1.05$ and rise at $z_c > 1.05$ for ultracentral collisions [35], I parametrized ρ_0 as

$$\rho_0 = \frac{1}{f_{\rm uc}} \left[\frac{a_{33} \sqrt{s_{NN}}^{a_{34}}}{1 + f_d \frac{M_{\rm ch}}{a_{35}}} - a_{36} \ln^2 \left(\frac{z_c}{a_{37}} \right) \right],$$

$$f_{\rm uc} = \left[1 - \frac{a_{38}}{z_c} \sqrt{\frac{2}{\pi}} \frac{\exp\left(-\frac{(z_c - a_{39})^2}{2a_{38}^2}\right)}{\operatorname{erfc}\left(\frac{z_c - a_{39}}{\sqrt{2} a_{38}}\right)} \right]^{a_{40}}. \tag{22}$$

Factor $f_{\rm uc}$ [35,36] is close to unity at $z_c \leqslant a_{38} \approx 1.1$ and decreases at $z_c > a_{39}$. So, it increases ρ_0 at $z_c > a_{39}$ and therefore increases $\langle p_{\rm T} \rangle$ for ultracentral events as in Refs. [35,36]. Parameter a_{35} is used to describe the observed slightly different centrality dependence of $\langle p_{\rm T} \rangle$ in Xe-Xe and Pb-Pb collisions, which is due to the nonsphericity of ^{129}Xe nuclei [34].

So, the parametrizations in Eqs. (16)–(22) allow us to determine the aforementioned (in Sec. II) more than 600 independent values for $V, V_1, V_2, T, k, e_2, n, f_S, r_{xy}$, and ρ_0 by means of about 40 constants.

I also parametrized other ingredients of BWTPM. The energy dependences of parameter $f_{\rm hyp}$ from Eqs. (11) and (12) and of the global normalization f_N are given as

$$f_N = a_N[1 + (a_{41}/\sqrt{s_{NN}})^{a_{42}}], \quad f_{\rm hyp} = \sqrt{s_{NN}}/a_{43}, \tag{23}$$

where $a_N = 1$ is assumed for Pb-Pb collisions at $\sqrt{s_{NN}} = 5.02$ TeV, and for other used data sets the values of a_N are defined relative to this one. As mentioned in Sec. II, it is assumed that the parameter ρ_2 as well as the functions $v_{2t}(p_{\rm T})$ and $v_{2p}(p_{\rm T})$ are proportional to ε_2 in order to ensure the relation $v_2 \sim \varepsilon_2$ [13–16]. A weak energy dependence of ρ_2 is parametrized as

$$\rho_2 = \varepsilon_2 a_{44}/\sqrt{s_{NN}}^{a_{45}}. \tag{24}$$

Functions $v_{2t}(p_{\rm T})$ and $v_{2p}(p_{\rm T})$ are responsible mainly for the description of the high-$p_{\rm T}$ behavior of elliptic flow v_2. For their dependence on $p_{\rm T}$, $\sqrt{s_{NN}}$, and $M_{\rm ch}$ I use

$$v_{2t}(p_{\rm T}) = \varepsilon_2 \frac{a_{46}}{y} \frac{x^z}{1 + t^2}, \quad v_{2p}(p_{\rm T}) = \varepsilon_2 \frac{a_{47}}{y} \frac{x^z}{1 + t^2}, \tag{25}$$

where $t = p_2/p_{\rm T}$, $x = \text{GeV}/m_{\rm T}$, $y = 1 + a_{48} m/\sqrt{s_{NN}}$, $z = a_{49} - a_{50} \ln z_c$, and parameter p_2 depends on the particle type. The latter can be expressed via the particle mass m as follows

TABLE I. Particle-type dependent model parameters.

Parameter	$\pi^{\pm}$, π^0	$K^{\pm}$, K^0_S	p, $\overline{p}$	η	ρ^0	K^{*0}, $\overline{K}^{*0}$	$\phi(1020)$	Λ, $\overline{\Lambda}$	Ξ^-, $\overline{\Xi}^+$	Ω^-, $\overline{\Omega}^+$	D^0, $D^{\pm}$	J/ψ	Λ_c^+, $\overline{\Lambda}_c^-$
$f_{\rm BW}$	1	0.993	3.76	1.26	2.18	2.23	1.66	10.96	7.08	8.29	192	1500	3600
f_1	1	0.085	0.00015	0	0	0	0	0	0	0	0	0	0
f_2	1	0.528	0.041	0.490	0.360	0.163	0.117	4.70	1.64	0.428	0.735	0.111	6.0
c_1	1.30	1.43	3.06										
$\tilde{e}_1$ (GeV)	0.065	0.099	0.361										
h_n	1	1	1	1	1	1	1	1.30	1.30	1.30	1	1.14	1.20

(m_π is the $\pi^{\pm}$ mass):

$$\frac{p_2}{\text{GeV}/c} = \begin{cases} a_{51} + a_{52}\left(1 - \frac{m_\pi}{m}\right)\ln\left(\frac{a_{53}}{m}\right) & \text{for mesons,} \\ a_{54} + a_{55}\exp\left(\frac{a_{56}}{m}\right) & \text{for baryons,} \\ a_{57} & \text{for } J/\psi. \end{cases} \tag{26}$$

The parametrization for mesons is inaccurate for J/ψ.

The particle type dependence of parameter c_2 can be expressed by a simple relation,

$$c_2 = 1 + \frac{m}{\text{GeV}/c^2}\begin{cases} a_{58}H(m - m_\pi) & \text{for mesons,} \\ a_{59}H(m - m_p) & \text{for baryons,} \end{cases} \tag{27}$$

where m_p is the proton mass and the step function H is defined as $H(x) = 0\,(1)$ for $x \leqslant (>)\ 0$. So $c_2 = 1$ for pions and (anti)protons. Larger a_{59} with respect to a_{58} is needed to describe the baryon yields. Note that the different parametrizations for mesons and baryons in Eqs. (26) and (27) indicate the difference in production mechanisms of these hadrons containing two and three (anti)quarks, respectively.

Parameter e_1 shows a centrality dependence significant mainly for pions. It can be described by

$$e_1 = \frac{\tilde{e}_1}{1 + \sqrt{f_p/\sqrt{s_{NN}}}}\left(1 + \frac{m_\pi}{m}\frac{a_{60}}{M_{\rm ch} + a_{23}}\right), \tag{28}$$

where parameter $\tilde{e}_1$ depends on the particle species. Parameter f_p is nonzero for the (anti)proton only to better describe its $p_{\rm T}$ spectra at RHIC energies. Additional normalization parameter $f_{\rm D}$ is used for $D^{\pm}$ mesons to describe their lower yield with respect to the D^0 meson.

V. FITTED DATA AND PARAMETERS

Thus, all the ingredients of the BWTPM are presented in previous sections. To determine the values of its free parameters, a global simultaneous fit is performed of the combined data on various hadrons' midrapidity $p_{\rm T}$ spectra, $\langle p_{\rm T}\rangle$, and v_2 for different centrality classes in Pb-Pb collisions at energies $\sqrt{s_{NN}} = 2.76$ and 5.02 TeV [18,34,35,37–62] and in Xe-Xe collisions at 5.44 TeV [33,63–65]. To check the validity of BWTPM for other colliding nuclei and at much lower energies, this fit also includes the $p_{\rm T}$ spectra and v_2 for $\pi^{\pm}$, $K^{\pm}$, and $p(\overline{p})$ measured in Au-Au collisions at $\sqrt{s_{NN}} = 200$ GeV [66,67], and the $p_{\rm T}$ spectra for $\pi^{\pm}$ and $K^{\pm}$ measured in Au-Au collisions at 39 and 27 GeV [68], in UU collisions at 193 GeV [69], and in Cu-Cu collisions at 200 GeV [70]. In the last four cases the proton data not included since they are not corrected for the contribution from weak decays of hyperons. The resulting ratio χ^2/NDF for this global fit (in the root framework [28]) is 6738/13408. Values for the fitting parameters are given in Tables I–III. Parameters $f_{\rm BW}$, f_1, and f_2 for $\pi^{\pm}$ and π^0 are fixed equal to unity. Note that the fit uses the data of prompt D and J/ψ mesons and Λ_c baryons, not including contributions from decays of heavier hadrons, containing b quarks. To describe the $p_{\rm T}$ spectra in Xe-Xe collisions [63,64], the right-hand side of Eq. (12) is scaled by a factor of 1.07 to account for a small normalization difference

TABLE II. Parameters a_1–a_{60} of Eqs. (16)–(28), f_r (is nonzero for ρ^0 and K^{*0} only) of Eq. (16), f_d (is nonzero for Xe-Xe only) of Eqs. (21) and (22), f_p (is nonzero for p and $\overline{p}$ only) of Eq. (28), and f_D for normalization of $D^{\pm}$ mesons.

a_1 (fm^3)	a_2 (fm^3)	a_3 (fm^3)	a_4	a_5 (GeV)	a_6	a_7	a_8	a_9 (GeV)	a_{10}	a_{11} (GeV)	a_{12}	a_{13}
6.15	17.62	0.015	2.0	0.1354	0.020	2.61	0.012	1.477	0.015	0.059	7.66	0.080
a_{14} (TeV)	a_{15}	a_{16}	a_{17} (GeV)	a_{18}	a_{19}	a_{20}	a_{21}	a_{22} (GeV)	a_{23}	a_{24}	a_{25}	a_{26}
0.027	10.85	0.80	35.0	3.60	0.92	2.50	0.53	24.0	5.0	0.341	0.070	0.0042
a_{27}	a_{28}	a_{29}	a_{30}	a_{31} (TeV)	a_{32}	a_{33}	a_{34}	a_{35}	a_{36}	a_{37}	a_{38}	a_{39}
0.782	0.159	1.56	6.63	0.166	1.80	0.984	0.083	5100	0.014	0.81	0.014	1.103
a_{40}	a_{41} (TeV)	a_{42}	a_{43} (TeV)	a_{44}	a_{45}	a_{46}	a_{47}	a_{48}	a_{49}	a_{50}	a_{51}	a_{52}
0.301	0.02	0.52	21.5	0.386	0.131	6.13	2.13	0.166	0.689	0.042	3.04	1.14
a_{53} (GeV)	a_{54}	a_{55}	a_{56} (GeV)	a_{57}	a_{58}	a_{59}	a_{60}	f_r, ρ^0	f_r, K^{*0}	f_d, Xe-Xe	f_p (TeV)	f_D
0.76	1.60	0.05	3.63	2.67	0.305	0.595	1.70	0.112	0.112	0.133	0.009	0.45

TABLE III. Normalization parameter a_N defined in Eq. (23) for all considered collision systems. Corresponding $\sqrt{s_{NN}}$ values are given in units of TeV.

	Pb-Pb		Xe-Xe		Au-Au		UU	Cu-Cu
$\sqrt{s_{NN}}$	5.02	2.76	5.44	0.2	0.039	0.027	0.193	0.2
a_N	1	1.044	0.986	1.008	1.003	0.973	1.110	0.965

between the measured p_T spectra of identified [63] and unidentified charged particles [64]. Note also that parameters a_{24}–a_{32} and a_{44}–a_{57} are resposible mainly for the elliptic flow. Only some of them entering in Eq. (24) influence the azimuthally integrated p_T spectra due to the ρ_2 contribution into the radial flow velocity Eq. (5). This contribution is small and decreases with increasing energy, according to Eq. (24). So, its influence on p_T spectra is negligible at high energies and becomes sizable (at most about several % at high p_T) only for Au-Au collisions at low energies $\sqrt{s_{NN}} = 27$ and 39 GeV. It should be noted that all the parameters listed

in Tables I–III have reasonable fitting uncertainties and are important for describing the data. For instance, the small parameter $a_{26} = 0.0042 \pm 0.0003$ is necessary for fitting v_2 for peripheral collisions. The global fit with $a_{26} = 0$ has $\chi^2 = 7140$ and significantly overestimates the v_2 data (shown in Fig. 14) at $M_{ch} < 40$ and $x_c > 0.7$.

VI. DISCUSSION OF THE RESULTS

A. Hadrons p_T spectra, integrated yields, and $\langle p_T \rangle$

First, I present several plots to illustrate the results and quality of the p_T-spectra fits. Figure 3 displays the fits of different data sets with highest p_T reached in central Pb-Pb collisions. To demonstrate the quality of the fits, the data points have been divided by the corresponding fit function values, and these ratios are also plotted in the bottom panel. Generally, the quality is good within the data uncertainties. Figures 4–6 display the main fits of the centrality dependent spectra for the most abundantly produced pions, kaons, and protons. The fit quality is almost always very good. This is true also for the fits of p_T spectra of all considered other particle species. The predictions for the 0–5% most central OO collisions (using $a_N = 1$) are shown in Fig. 5. Note that Figs. 3 and 4 repeat the similar ones of Ref. [1] to show that the present version of BWTPM with much fewer fitting parameters gives similar fit quality. Also, it is checked that the relative contributions of the BW, Ts, and Po components of the present modelto the p_T spectra are similar to the ones given in Ref. [1]. As shown in Table I, the contribution of the Ts component is nonzero only for pions, kaons, and protons, which have significant feedback from the resonance decays.

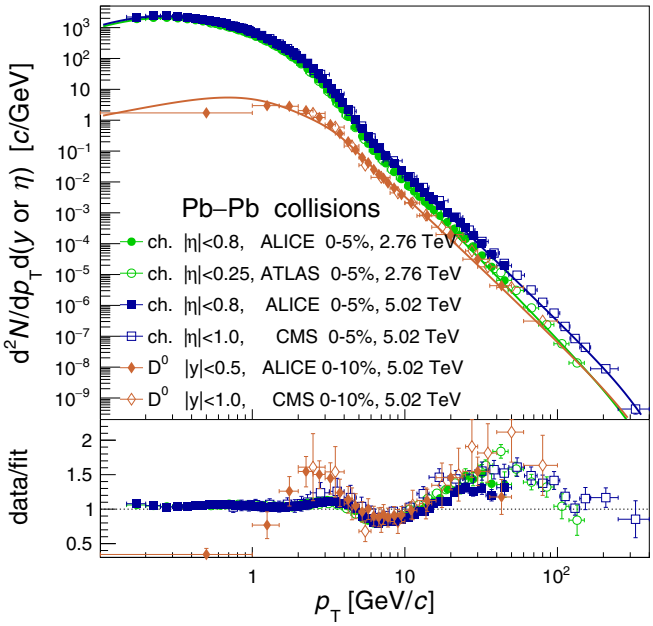


FIG. 3. Fit of p_T spectra with highest p_T reached in Pb-Pb collisions for charged particles at $\sqrt{s_{NN}} = 2.76$ TeV [38,41] and 5.02 TeV [38,42] and for D^0 at $\sqrt{s_{NN}} = 5.02$ TeV [43,48].

Then, Fig. 7 shows a good agreement of the model calculations (using the parameter values given in Sec. V) for the ratios of p_T spectra of different hadrons with the ALICE data obtained in central and peripheral Pb-Pb collisions. These ratios, like the other ones given in Ref. [1], demonstrate more clearly the effect of hadron production mechanisms on the p_T spectra. The peaks at $p_T \approx 2$–7 GeV/c are related to the radial flow, which is stronger for heavier particles and more central collisions. The ratios with the short-lived K^{*0} and ρ^0 resonances show the suppression of their yields for low-p_T and central collisions, according to Eq. (16). To demonstrate the collision system and energy dependence of particle ratios, the left panels of Fig. 7 show the model calculations for 0–10% centrality Au-Au (dashed lines) and Cu-Cu (dotted lines) collisions at $\sqrt{s_{NN}} = 200$ GeV. Both dependencies are not strong and appear at moderate p_T. Note that the hadron p_T spectra in Eq. (9) have a power-law behavior $\propto p_T^{2-n}$ at high p_T. Hence, the ratios for all hadrons, which have $h_n = 1$ in Table I, reach a plateau (independent of the collision system, centrality, and $\sqrt{s_{NN}}$) at high p_T where parameter n in Eq. (19) depends only on $\sqrt{s_{NN}}$. The plateau is simply defined by the ratio of factors $(2J+1)f_2$ with f_2 given in Table I. It is true also for the ratios between hyperons that have the same h_n. For example, the ratio η/π^0 reach a plateau value of 0.49, which is compatible with the measurement $0.457 \pm 0.013 \pm 0.018$ [58] and with the empirical fit result 0.487 ± 0.024 [71].

Figure 8 displays the ratios of the p_T-integrated yields of various hadrons as a function of the charged-particle multiplicity M_{ch} [defined by Eq. (2)] in Pb-Pb collisions. It is well known that such ratios have smooth behavior versus M_{ch} and are almost independent of the collision system and energy [11,33]. Corresponding ratios in Xe-Xe collisions at $\sqrt{s_{NN}} = 5.44$ TeV [33] are not shown in Fig. 8 for clarity. The model curves in this case, as well as for OO collisions at $\sqrt{s_{NN}} = 5.36$ TeV, coincide practically with the ones for Pb-Pb at $\sqrt{s_{NN}} = 5.02$ TeV. The model describes well all the presented ratios. In particular, it describes the observed enhancement of yields of hadrons containing strange (anti)quarks with respect to pion yields when going from peripheral to central

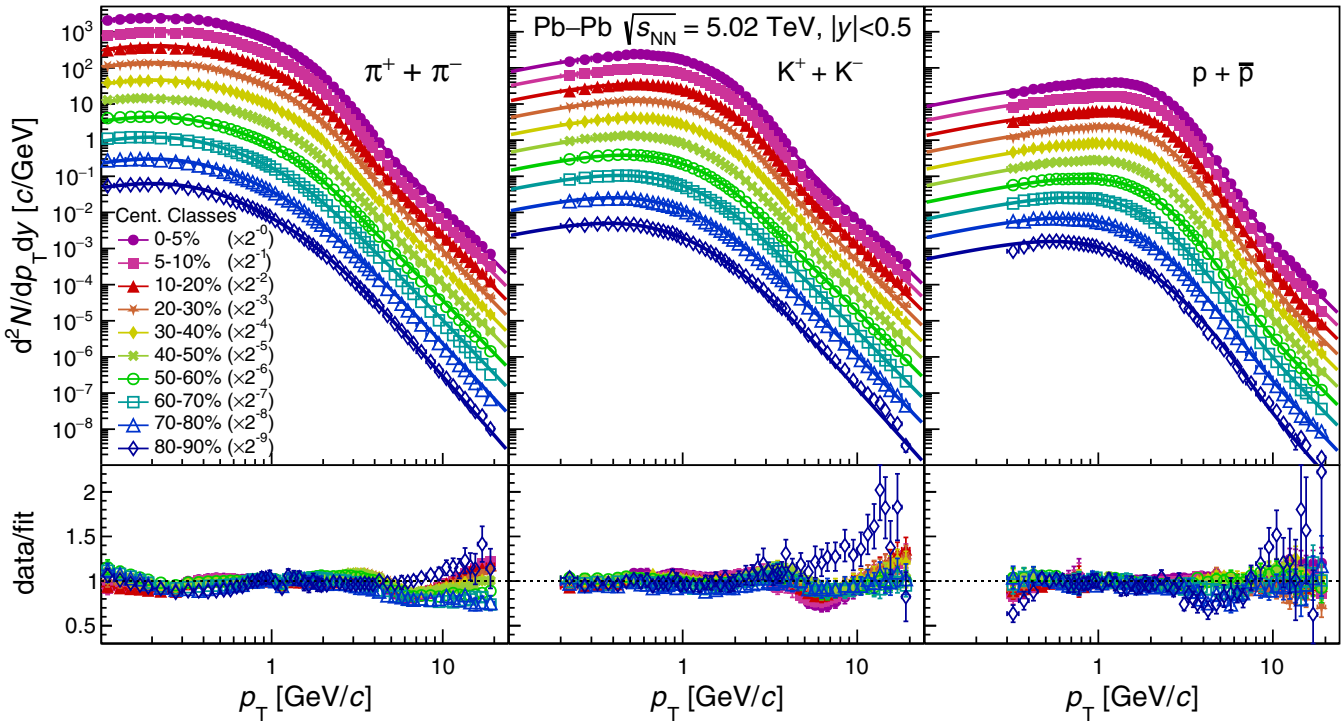


FIG. 4. Fit of pion, kaon, and proton p_T spectra at $|y| < 0.5$ for different centrality classes (centrality intervals) in Pb-Pb collisions at $\sqrt{s_{NN}} = 5.02$ TeV [18]. The data points and fitting curves in the top panels are scaled, for better visibility, by the numbers given in the parentheses.

collisions. Enhancement is stronger for hadrons containing more strange (anti)quarks, according to Eq. (20). Figure 8 displays also the suppression of K^{*0} and ρ^0 resonance yields when going from peripheral to central collisions. It is the manifestation of the low-p_T suppression of these resonances (see Fig. 7) due to the rescatterings of their decay products in

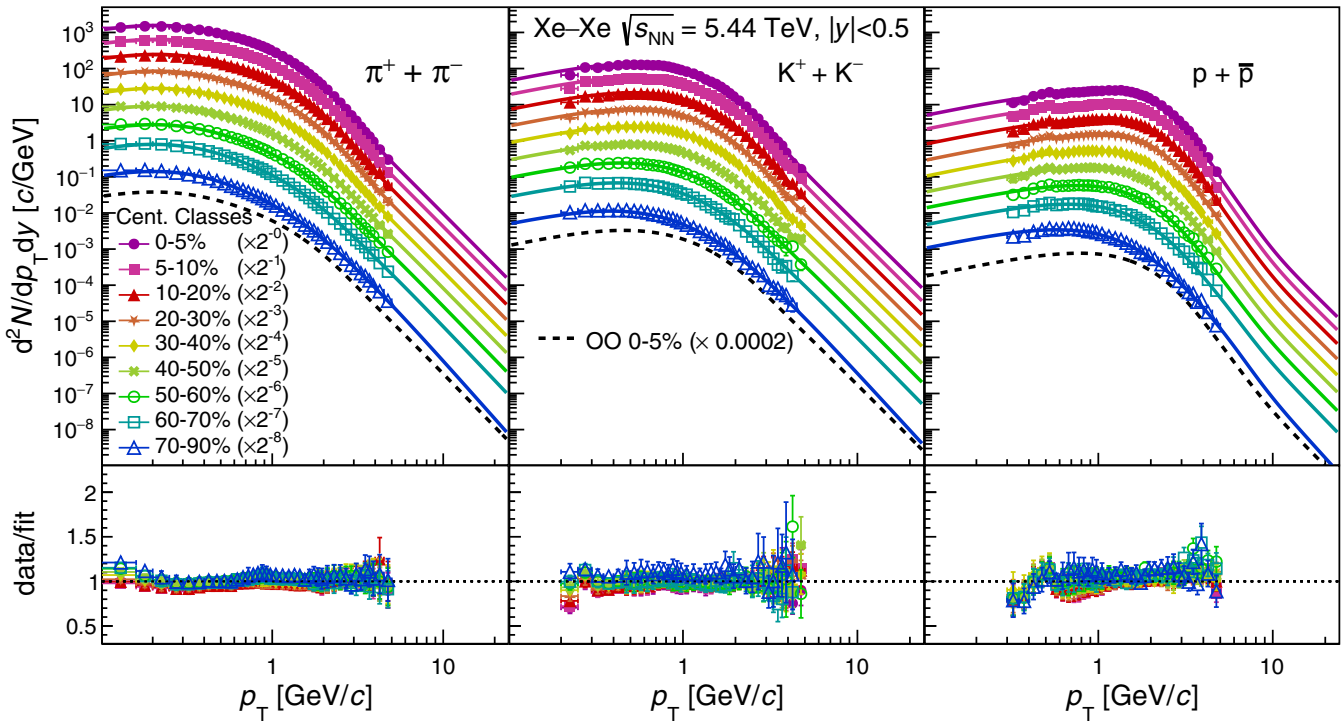


FIG. 5. Similar to Fig. 4 but for Xe-Xe collisions at $\sqrt{s_{NN}} = 5.44$ TeV [63]. In addition, the dashed lines in the top panels show the predictions (scaled down by 0.0002 for better visibility) for 0–5% centrality OO collisions at $\sqrt{s_{NN}} = 5.36$ TeV.

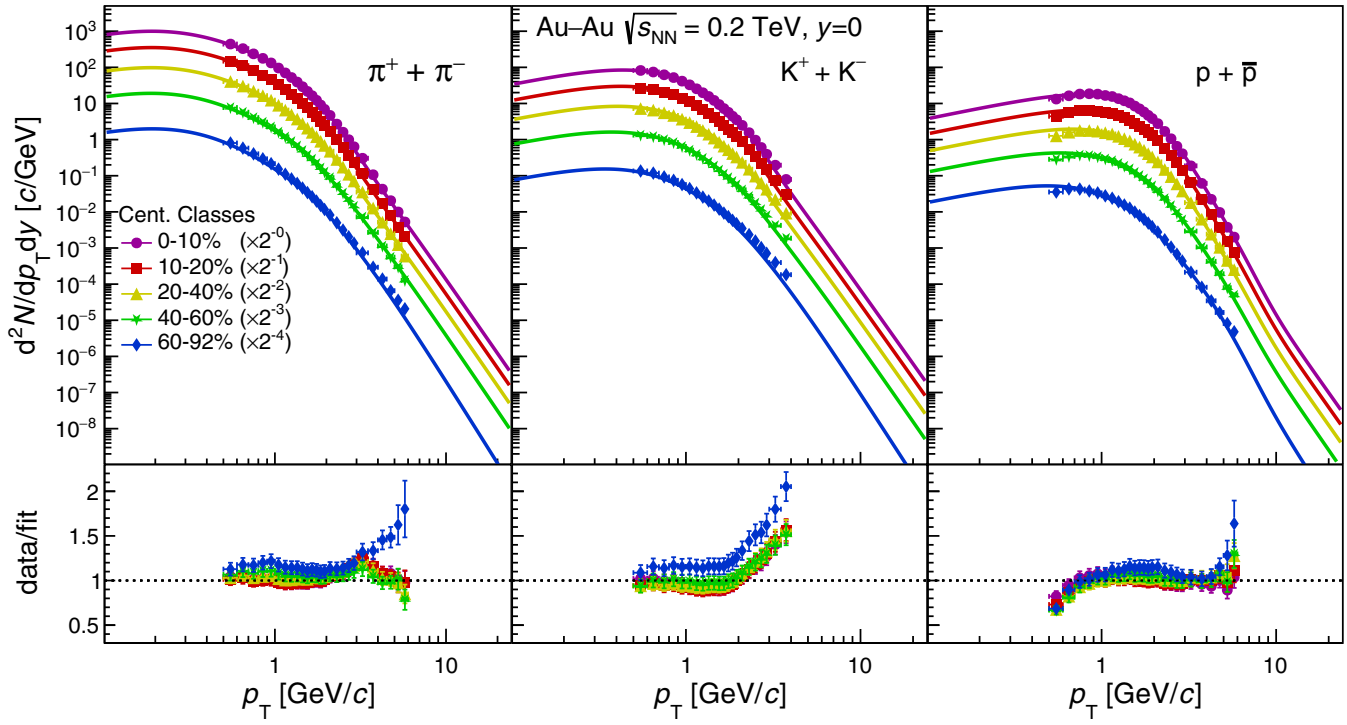


FIG. 6. Similar to the Fig. 4 but for Au-Au collisions at $\sqrt{s_{NN}} = 0.2$ TeV [66].

the hadronic medium. The ϕ resonance does not have such a suppression since it lives longer than this medium [11].

Next, Fig. 9 shows the fit of the data on charged-particle $\langle p_T \rangle$ versus M_{ch} in Pb-Pb and Xe-Xe collisions [34]. These data involve much more values of M_{ch} than the p_T-spectra measurements [38,64]. The prediction for OO collisions is shown too. The sharp rise in model curves at very high M_{ch}, related to factor f_{uc} of Eq. (22), is demonstrated in detail in Fig. 10 with the Pb-Pb data [35] at $\sqrt{s_{NN}} = 5.02$ TeV for the normalaized $\langle p_T \rangle$ and M_{ch} to the corresponding values for 0–5% centrality. The predictions for Pb-Pb at $\sqrt{s_{NN}} = 2.76$ TeV, Xe-Xe at $\sqrt{s_{NN}} = 5.44$ TeV, and OO at $\sqrt{s_{NN}} = 5.36$ TeV are also shown. Overall, a good description of the data can be seen.

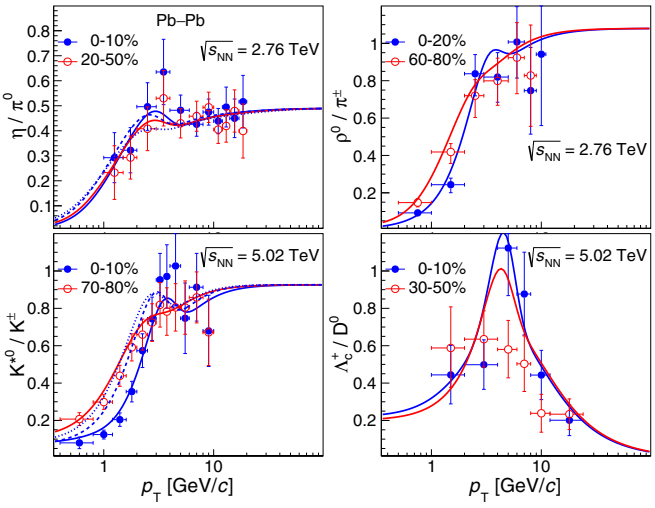


FIG. 7. Comparison of the model calculations for the ratios of different particle p_T spectra with the data of central and peripheral Pb-Pb collisions at $\sqrt{s_{NN}} = 2.76$ and 5.02 TeV [40,58–60]. The dashed (dotted) lines show the ratios for 0–10% centrality Au-Au (Cu-Cu) collisions at $\sqrt{s_{NN}} = 200$ GeV.

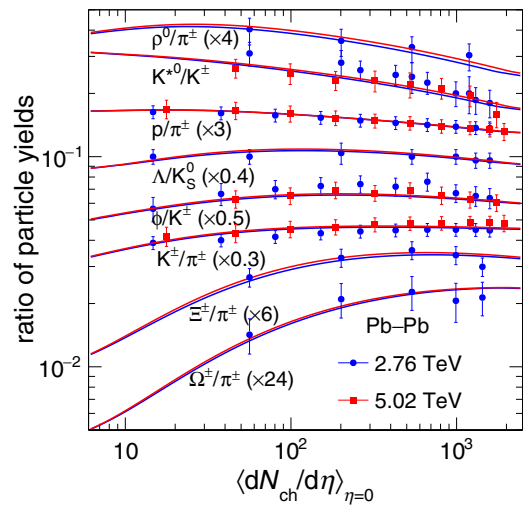


FIG. 8. Comparison of the model calculations for the ratios of different particle p_T-integrated yields as a function of the charged-particle multiplicity density with the measurements in Pb-Pb collisions at $\sqrt{s_{NN}} = 2.76$ and 5.02 TeV [17,18,40,44–46].

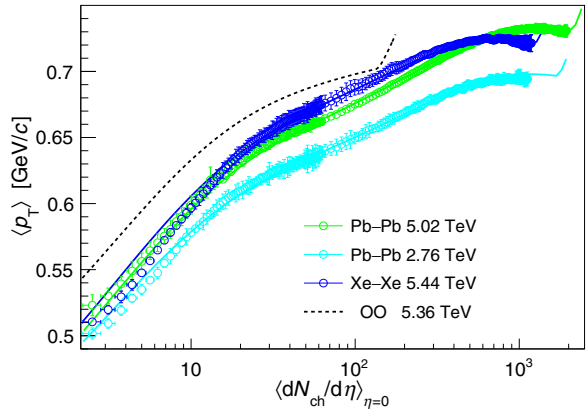


FIG. 9. Fit of charged particles $\langle p_{\mathrm{T}} \rangle$ as a function of their multiplicity density in Pb-Pb collisions at $\sqrt{s_{NN}} = 2.76$ and 5.02 TeV, and in Xe-Xe collisions at $\sqrt{s_{NN}} = 5.44$ TeV [34]. Dashed line shows the prediction for OO collisions at $\sqrt{s_{NN}} = 5.36$ TeV.

B. Hadrons' p_{T} differential and averaged v_2

It should be noted that the elliptic flow v_2 data considered in present paper [33,52–57,61,62,65,68] were measured mostly by the two-particle cumulant method and partly by other similar methods that give compatible results within the data uncertainties. This method assumes a minimum pseudorapidity gap $\Delta\eta$ between the two particles, meant to suppress the nonflow correlations, for which the largest available value in any dataset used was chosen.

Figures 11–13 demonstrate the fits of p_{T} differential v_2 for various hadrons and different centralities in Pb-Pb [52–55] and Au-Au [68] collisions, as well as some features of such data [11,61]. A similarly good fit is also obtained for the v_2 data in Xe-Xe collisions at $\sqrt{s_{NN}} = 5.44$ TeV [33,65]. The v_2 (p_{T}) has a wide peak at $p_{\mathrm{T}} \approx$ 1–7 GeV/c, whose height increases with the percentage of centrality up to ∼50% and

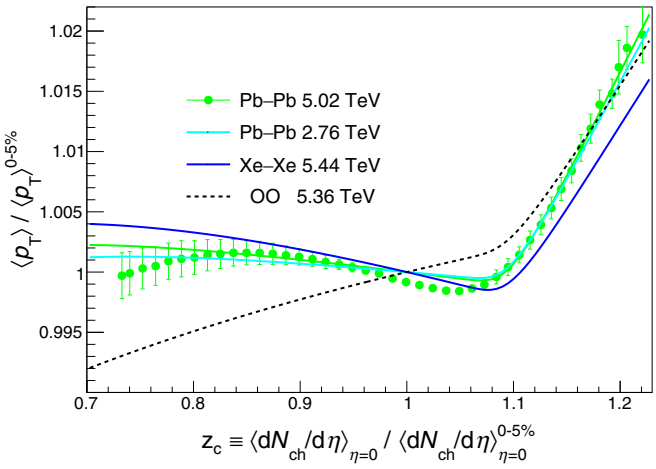


FIG. 10. Fit of charged particles normalized $\langle p_{\mathrm{T}} \rangle$ as a function of their normalized multiplicity density z_c in Pb-Pb collisions at $\sqrt{s_{NN}} = 5.02$ TeV [35]. The predictions for Pb-Pb at $\sqrt{s_{NN}} = 2.76$ TeV, Xe-Xe at $\sqrt{s_{NN}} = 5.44$ TeV, and OO at $\sqrt{s_{NN}} = 5.36$ TeV are shown too.

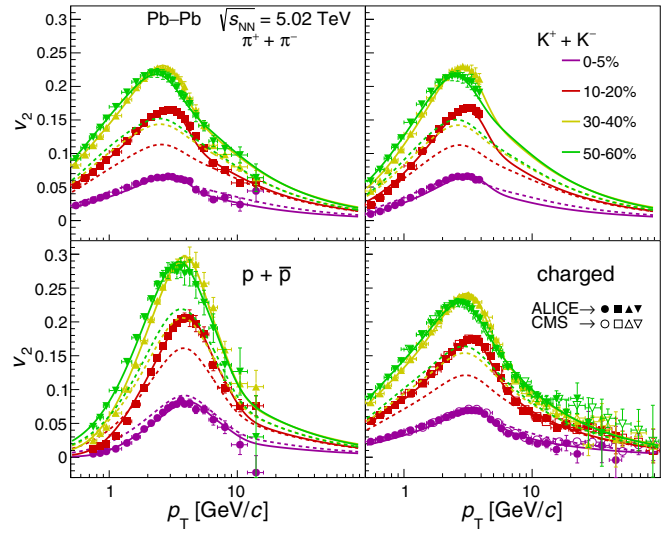


FIG. 11. Fit of pion, kaon, proton, and charged-particle v_2 as a function of p_{T} in Pb − Pb collisions at $\sqrt{s_{NN}} = 5.02$ TeV for four centrality intervals, measured by ALICE [53,54] and CMS [55] experiments. The dashed lines show the predictions for OO collisions at $\sqrt{s_{NN}} = 5.36$ TeV.

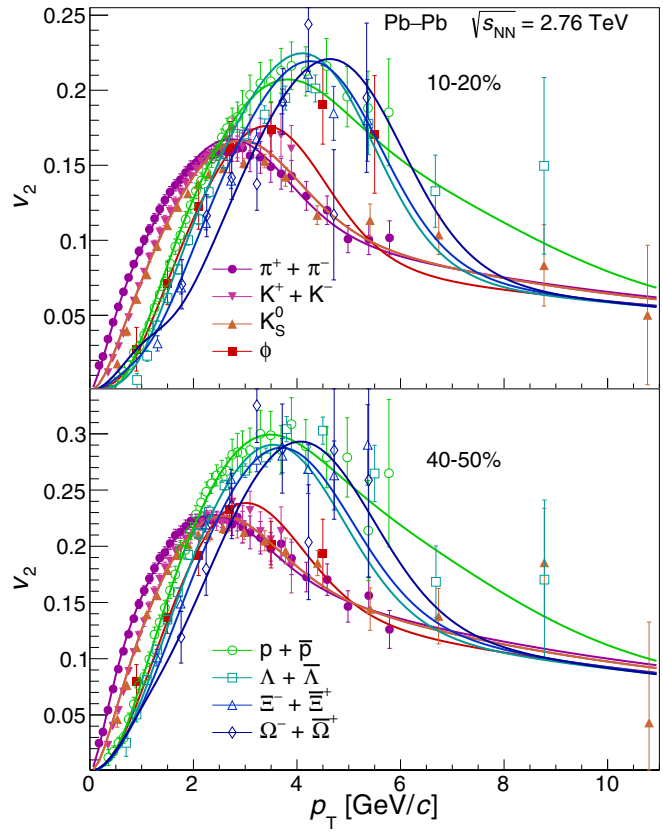


FIG. 12. Fit of v_2 for different particles as a function of p_{T} in Pb − Pb collisions at $\sqrt{s_N N} = 2.76$ TeV for centrality intervals 10–20% and 40–50% [52].

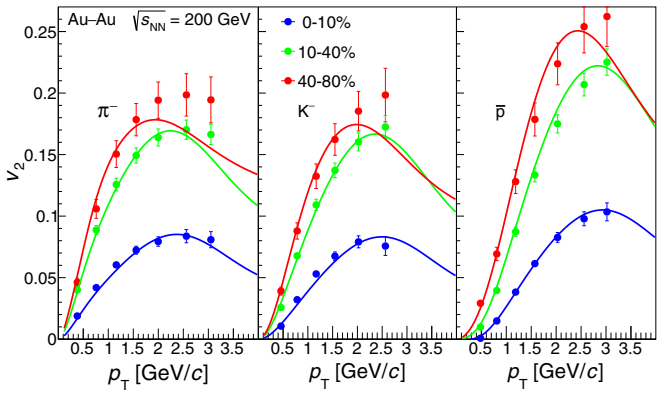


FIG. 13. Fit of v_2 for π^-, K^-, and $\overline{p}$ as a function of p_T in Au-Au collisions at $\sqrt{s_{NN}} = 200$ GeV for three centrality intervals [68].

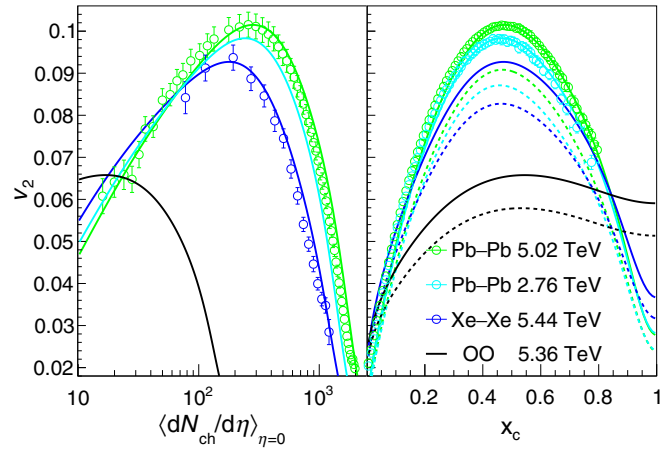


FIG. 14. Fit of charged-particle v_2, averaged in the p_T range $0.2 < p_T < 3.0$ GeV/c, as a function of multiplicity density [62] (left panel) and x_c [54] (right panel) in Pb-Pb collisions at $\sqrt{s_{NN}} = 5.02$ and 2.76 TeV, and in Xe-Xe collisions at $\sqrt{s_{NN}} = 5.44$ TeV. The black lines show the predictions for OO collisions at $\sqrt{s_{NN}} = 5.36$ TeV. The dashed lines correspond to v_2 averaged in the p_T range $0 < p_T < 20$ GeV/c .

then decreases for more peripheral collisions. This is related to the collision geometry [61] and can be explained in the present model by the similar centrality dependence of ε_2, defined by Eqs. (7) and (21). The peak is shifted to higher p_T for heavier particles. It is the well-known mass-ordering effect caused due to the radial flow [11,61]. Such a shift also occurs with increasing centrality (or M_{ch}) due to the increasing radial flow velocity β_T in Eq. (5) caused by the decreasing exponent k defined in Eq. (17). Another known feature of v_2 is the meson-baryon particle type grouping [11,61], clearly visible in Fig. 12. This is described in present model by using different parametrizations for mesons and baryons in Eq. (26). Another effect is the increase of v_2 with $\sqrt{s_{NN}}$ [11], which can be seen by comparing Figs. 11 and 13. It is mainly related to the increase of β_T caused by the decreasing k in Eq. (17) with increasing $\sqrt{s_{NN}}$ (or M_{ch}). For the fit shown in Fig. 13 the π^-, K^-, and $\overline{p}$ dataset was used since it includes more data-points than the π^+, K^+, and p dataset [68]. Note also that the dashed lines in Fig. 11 show the predictions for OO collisions at $\sqrt{s_{NN}} = 5.36$ TeV.

It is important to note that the BW term of the present model [see Eq. (10)] gives, for most of considered hadrons, the main contribution to v_2 in the lower part of its whole p_T region up to the center of the peak. The Ts and Po terms, with the use of Eq. (25), describe v_2 in the rest of this region. However, for hadrons containing heavy quarks, for which the Ts term is zero and the BW term is suppressed by a factor $\sim \exp(-m_T/T)$, the Po contribution to v_2 dominates everywhere (as for p_T spectra [1]).

Finally, let us discuss the p_T-averaged v_2, defined via Eq. (1) with integration by p_T in the numerator and denominator. Figure 14 shows the fit for the charged-particle v_2, averaged in the p_T range $0.2 < p_T < 3.0$ GeV/c, as a function of M_{ch} [62] (left panel) and centrality fraction x_c (defined in Sec. III) [54] (right panel). Although both datasets were obtained by the two-particle cumulant method, they are independent measurements since Refs. [54,62] use $\Delta\eta > 1.4$ and $\Delta\eta > 1$, respectively. Very good fits of the Pb-Pb and Xe-Xe data can be seen in Fig. 14. The black lines show the predictions for OO collisions at $\sqrt{s_{NN}} = 5.36$ TeV.

For comparison, dashed lines are shown corresponding to v_2 averaged in the much larger p_T range $0 < p_T < 20$ GeV/c. The left panel of Fig. 14 shows that the model describes well the different M_{ch} (or centrality) dependences of v_2 in Xe-Xe and Pb-Pb collisions. This is due to the presence of the parameter f_d, related to the nonspherical form of the ^{129}Xe nucleus, and of the A dependence in Eq. (21). Also important is the smaller β_T [caused by the larger k from Eq. (17)[for collisions of smaller nuclei. These A dependence and smaller β_T are the main reasons for the lower values and flatter centrality (or M_{ch}) dependence of the predicted v_2 in OO collisions with respect to Pb-Pb collisions, shown in Figs. 11 and 14.

C. Study of hadrons not used in the global fit

To demonstrate the ability of BWTPM to describe the data for other hadrons, not used in the global fit, here I consider the ALICE measurements for the p_T spectra of baryon resonances $\Sigma(1385)^+$ and $\Sigma(1385)^-$ [72] and $\Lambda(1520)$ [73] in Pb-Pb collisions (the sum of the particle and antiparticle yields was measured in each case). The data show that the yields of these short-lived resonances are suppressed in central collisions. This suppression can be quantified via the parameter f_r from Eq. (16), as for the K^{*0} and ρ^0 resonances discussed above. Since the data [72,73] on baryon resonances are scarce, especially at low p_T, one can use for their parameter f_r the value given in Table II. Then, to fit these data, there are left only three particle-specific free parameters: f_{BW}, f_2, and h_n. The combined fit of the data [72], shown in the left panel of Fig. 15, gives $\chi^2/\text{NDF} = 6.8/51$, $f_{BW} = 6.14$, $f_2 = 0.49$, and $h_n = 1.25$. Note that the value of h_n is close to the one given in Table I for hyperons. The $\Lambda(1520)$ data [73] are very scarce at high p_T, so the fitting function is almost insensitive to the parameter h_n. The fit of these data, using fixed $h_n = 1.25$

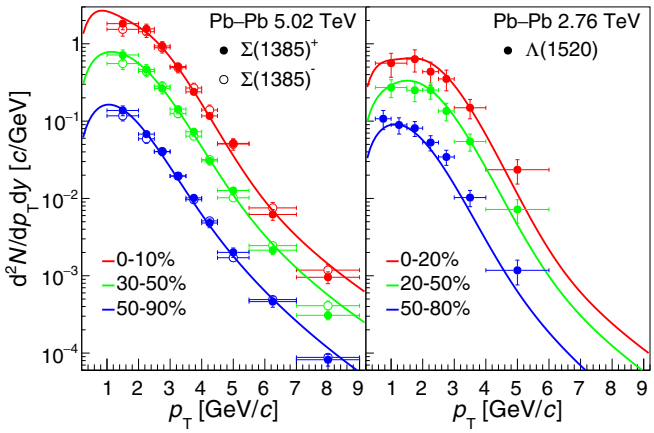


FIG. 15. Fit of p_{T} spectra of $\Sigma(1385)^{\pm}$ [72] (left panel) and $\Lambda(1520)$ [73] (right panel) in Pb-Pb collisions at $\sqrt{s_{NN}} = 5.02$ and 2.76 TeV, respectively, for three centrality classes.

and two free parameters, gives $\chi^2/\mathrm{NDF} = 5.4/17$, $f_{\mathrm{BW}} = 12.8$, $f_2 = 0.20$, and is displayed in the right panel of Fig. 15.

So, by fitting only few particle-specific parameters, BWTPM allows us to describe the data for new (not considered here) particles produced in AA collisions at different centralities and energies.

VII. CONCLUSIONS

Thus, a more general and parametrized version of BWTPM [1] is presented, which has much fewer free parameters, but successfully describes not only the midrapidity p_{T} spectra, but also elliptic flow v_2 of various hadrons with arbitrary p_{T} in AA collisions for any centrality at the LHC energies. It is shown that the model also works at much lower RHIC energies. For all considered particles, from pions to charmonia, BWTPM allows us to easily calculate the midrapidity p_{T} spectra and v_2 for new AA collisions with any A and centrality at high energies. Predictions are given for the OO collisions carried out recently at the LHC. However, for collisions of isobars and other deformed nuclei, shape-specific parameters should be introduced, such as the f_d parameter used above for Xe-Xe collisions. To calculate the p_{T} spectra or v_2 for new particles, not considered in this study, one needs some data (e.g., p_{T} spectrum for at least one centrality or $\langle p_{\mathrm{T}} \rangle$ versus centrality) to fix the particle-specific parameters, as shown for the strange baryon resonances in Sec. VI C.

In the future, it is planned to employ BWTPM to describe the available data on the production of light nuclei (such as deuteron and helion) in AA collisions.

BWTPM can be efficiently used by experimenters to quickly check new data on hadron p_{T} spectra and v_2. Similarly, the simple parametrization for the charged-particle multiplicity density at midrapidity in AA or pp collisions presented in Sec. III can also be used.

ACKNOWLEDGMENTS

I thank Jurgen Schukraft for valuable comments on the BWTPM parametrization. I also thank the anonymous referee for important comments that led to further discussion of deformed nucleus collisions and BWTPM parameters as well as the addition of Sec. VI C.

DATA AVAILABILITY

The data supporting the findings of this article are openly available [17–27,33–35,37–70,72,73].

[1] S. Grigoryan, Eur. Phys. J. A **57**, 328 (2021).
[2] E. Schnedermann, J. Sollfrank, and U. Heinz, Phys. Rev. C **48**, 2462 (1993).
[3] C. Tsallis, J. Stat. Phys. **52**, 479 (1988).
[4] S. Grigoryan, Phys. Rev. D **95**, 056021 (2017).
[5] J.-Y. Ollitrault, Phys. Rev. D **46**, 229 (1992).
[6] F. Retiere and M. A. Lisa, Phys. Rev. C **70**, 044907 (2004).
[7] K. Reygers, A. Schmah, A. Berdnikova, and X. Sun, Phys. Rev. C **101**, 064905 (2020).
[8] S. Voloshin and Y. Zhang, Z. Phys. C **70**, 665 (1996).
[9] A. M. Poskanzer and S. A. Voloshin, Phys. Rev. C **58**, 1671 (1998).
[10] H. Heiselberg and A.-M. Levy, Phys. Rev. C **59**, 2716 (1999).
[11] S. Acharya, *et al.* (ALICE Collaboration), Eur. Phys. J. C **84**, 813 (2024).
[12] S. Acharya, *et al.* (ALICE Collaboration), Eur. Phys. J. C **77**, 658 (2017).
[13] S. A. Voloshin and A. M. Poskanzer, Phys. Lett. B **474**, 27 (2000).
[14] J.-Y. Ollitrault, Eur J. Phys. **29**, 275 (2008).
[15] Z. Qiu and U. W. Heinz, Phys. Rev. C **84**, 024911 (2011).
[16] S. Acharya, *et al.* (ALICE Collaboration), Phys. Lett. B **846**, 137453 (2023).
[17] B. Abelev, *et al.* (ALICE Collaboration), Phys. Rev. C **88**, 044910 (2013).
[18] S. Acharya, *et al.* (ALICE Collaboration), Phys. Rev. C **101**, 044907 (2020).
[19] S. Acharya, *et al.* (ALICE Collaboration), Phys. Lett. B **790**, 35 (2019).
[20] S. Acharya, *et al.* (ALICE Collaboration), arXiv:2504.02505.
[21] B. Alver, *et al.* (PHOBOS Collaboration), Phys. Rev. C **83**, 024913 (2011).
[22] A. Adare, *et al.* (PHENIX Collaboration), Phys. Rev. C **93**, 024901 (2016).
[23] S. Acharya, *et al.* (ALICE Collaboration), Phys. Rev. C **109**, 014911 (2024).
[24] J. Adam, *et al.* (ALICE Collaboration), Eur. Phys. J. C **77**, 33 (2017).
[25] J. Adam, *et al.* (ALICE Collaboration), Phys. Lett. B **753**, 319 (2016).
[26] S. Acharya, *et al.* (ALICE Collaboration), Phys. Rev. D **108**, 072008 (2023).
[27] W. Thomé, *et al.* (Aachen-CERN-Heidelberg-Munich Collaboration), Nucl. Phys. B **129**, 365 (1977).

[28] R. Brun and F. Rademakers, Nucl. Instrum. Methods Phys. Res., Sect. A **389**, 81 (1997). http://root.cern/.
[29] M. S. Abdallah, *et al.*, Phys. Rev. C **105**, 014901 (2022).
[30] L. Adamczyk, *et al.* (STAR Collaboration), Phys. Rev. Lett. **115**, 222301 (2015).
[31] G. Giacalone, A. Mazeliauskas, and S. Schlichting, Phys. Rev. Lett. **123**, 262301 (2019).
[32] J. Cleymans, P. M. Lo, K. Redlich, and N. Sharma, Phys. Rev. C **103**, 014904 (2021).
[33] S. Acharya, *et al.* (ALICE Collaboration), Phys. Lett. B **784**, 82 (2018).
[34] S. Acharya, *et al.* (ALICE Collaboration), Phys. Lett. B **845**, 138110 (2023).
[35] A. Hayrapetyan, *et al.* (CMS Collaboration), Rep. Prog. Phys. **87**, 077801 (2024).
[36] F. G. Gardim, G. Giacalone, and J.-Y. Ollitrault, Phys. Lett. B **809**, 135749 (2020).
[37] J. Adam, *et al.* (ALICE Collaboration), Phys. Rev. C **93**, 034913 (2016).
[38] S. Acharya, *et al.* (ALICE Collaboration), J. High Energy Phys. 11 (2018) 013.
[39] J. Adam, *et al.* (ALICE Collaboration), Phys. Rev. C **95**, 064606 (2017).
[40] S. Acharya, *et al.* (ALICE Collaboration), Phys. Lett. B **802**, 135225 (2020).
[41] G. Aad, *et al.* (ATLAS Collaboration), J. High Energy Phys. 09 (2015) 050.
[42] V. Khachatryan, *et al.* (ATLAS Collaboration), J. High Energy Phys. 04 (2017) 039.
[43] A. Sirunyan, *et al.* (CMS Collaboration), Phys. Lett. B **782**, 474 (2018).
[44] B. Abelev, *et al.* (ALICE Collaboration), Phys. Rev. C **91**, 024609 (2015).
[45] B. Abelev, *et al.* (ALICE Collaboration), Phys. Rev. Lett. **111**, 222301 (2013).
[46] B. Abelev, *et al.* (ALICE Collaboration), Phys. Lett. B **728**, 216 (2014). **734**, 409 (2014).
[47] J. Adam, *et al.* (ALICE Collaboration), J. High Energy Phys. 03 (2016) 081.
[48] S. Acharya, *et al.* (ALICE Collaboration), J. High Energy Phys. 10 (2018) 174.
[49] A. Sirunyan, *et al.* (CMS Collaboration), Eur. Phys. J. C **78**, 509 (2018).
[50] M. Aaboud, *et al.* (ATLAS Collaboration), Eur. Phys. J. C **78**, 762 (2018).
[51] S. Acharya, *et al.* (ALICE Collaboration), J. High Energy Phys. 01 (2022) 174.
[52] B. Abelev, *et al.* (ALICE Collaboration), J. High Energy Phys. 06 (2015) 190.
[53] S. Acharya, *et al.* (ALICE Collaboration), J. High Energy Phys. 09 (2018) 006.
[54] S. Acharya, *et al.* (ALICE Collaboration), J. High Energy Phys. 07 (2018) 103.
[55] A. Sirunyan, *et al.* (CMS Collaboration), Phys. Lett. B **776**, 195 (2018).
[56] A. Sirunyan, *et al.* (CMS Collaboration), Phys. Lett. B **816**, 136253 (2021).
[57] S. Acharya, *et al.* (ALICE Collaboration), J. High Energy Phys. 10 (2020) 141.
[58] S. Acharya, *et al.* (ALICE Collaboration), Phys. Rev. C **98**, 044901 (2018).
[59] S. Acharya, *et al.* (ALICE Collaboration), Phys. Rev. C **99**, 064901 (2019).
[60] S. Acharya, *et al.* (ALICE Collaboration), Phys. Lett. B **839**, 137796 (2023).
[61] S. Acharya, *et al.* (ALICE Collaboration), J. High Energy Phys. 05 (2023) 243.
[62] S. Acharya, *et al.* (ALICE Collaboration), Phys. Rev. Lett. **123**, 142301 (2019).
[63] S. Acharya, *et al.* (ALICE Collaboration), Eur. Phys. J. C **81**, 584 (2021).
[64] S. Acharya, *et al.* (ALICE Collaboration), Phys. Lett. B **788**, 166 (2019).
[65] S. Acharya, *et al.* (ALICE Collaboration), J. High Energy Phys. 12 (2021) 152.
[66] A. Adare, *et al.* (PHENIX Collaboration), Phys. Rev. C **88**, 024906 (2013).
[67] L. Adamczyk, *et al.* (STAR Collaboration), Phys. Rev. C **96**, 044904 (2017).
[68] M. S. Abdallah, *et al.* (STAR Collaboration), Phys. Rev. C **105**, 064911 (2022).
[69] M. S. Abdallah, *et al.* (STAR Collaboration), Phys. Rev. C **107**, 024901 (2023).
[70] I. C. Arsene, *et al.* (BRAHMS Collaboration), Phys. Rev. C **94**, 014907 (2016).
[71] Y. Ren and A. Drees, Phys. Rev. C **104**, 054902 (2021).
[72] S. Acharya, *et al.* (ALICE Collaboration), Eur. Phys. J. C **83**, 351 (2023).
[73] S. Acharya, *et al.* (ALICE Collaboration), Phys. Rev. C **99**, 024905 (2019).